Additive Manufacturing 79 (2024) 103922

Contents lists available at ScienceDirect

Additive Manufacturing

journal homepage: www.elsevier.com/locate/addma

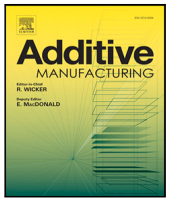

Research paper

On the size-dependent fatigue behaviour of laser powder bed fusion Ti-6Al-4V

Jieming S. Zhang [a,*], Yuanbo T. Tang [a], Ruining Jin [a], Andrew Lui [a], Patrick S. Grant [a], Enrique Alabort [b], Alan C.F. Cocks [c], Roger C. Reed [a,c]

[a] Department of Materials, University of Oxford, Parks Road, Oxford, OX1 3PH, United Kingdom
[b] Alloyed Ltd, Unit 15, Oxford Industrial Park, Yarnton, OX5 1QU, United Kingdom
[c] Department of Engineering Science, University of Oxford, Parks Road, Oxford, OX1 3PJ, United Kingdom

ARTICLE INFO

Keywords:
Titanium
Laser powder bed fusion
Fatigue
Size-dependency
X-ray computed tomography

ABSTRACT

A sample size effect which influences the fatigue behaviour of laser powder bed fusion Ti-6Al-4V is identified and quantified. Two cylindrical samples are considered: ∅ 1.3 mm and ∅ 2.0 mm. The larger specimen demonstrates better fatigue resistance particularly in the high-cycle regime, with the differing surface roughness contributing to this effect. It is also confirmed that processing-induced porosity can compromise the fatigue performance even when the initiation sites are surface defects. The larger contribution of porosity to the fatigue fracture process of the larger specimen results in a higher scatter in the fatigue life. Differences in microstructure do not seem to contribute strongly to the variation in fatigue properties of the two specimens, but we present some evidence that the coarser microstructure of the larger specimen promotes a stronger tolerance to defects and induces more tortuous crack paths which hinders fatigue crack growth.

1. Introduction

Metal additive manufacturing (AM) serves as a transformative route for the production of engineering components [1–3]. Its layer-by-layer manufacturing approach offers unprecedented geometrical freedom in design, which promises light-weight and functionalization of structures [4–6]. In general, the optimization of geometrical features requires sub-structures to be printed in different thicknesses. Thus, the variation in characteristic cross-sectional area together with a combination of processing parameters can introduce structural inhomogeneity within the component [7,8]. This can be detrimental to the mechanical integrity of the component, especially the fatigue behaviour — one of the most common failure mechanisms for many applications [9–11]. This can be regarded as the Archilles' heel of the AM process, limiting the adoption of the technology in these critical sectors. To unleash the full potential that AM promises, the influence of sample size on the fatigue properties must be better understood.

Ti-6Al-4V is one of the most commonly used alloys in aerospace and biomedical sectors [6,7,12]. Extensive research has been carried out on this alloy when manufactured by AM [7,13,14]. Among all the AM techniques, laser powder bed fusion (L-PBF) serves as a promising route to fabricate Ti-6Al-4V due to its fine resolution and high surface quality [3,15,16]. Hence, it is employed in this work. The microstructure and defect formation within L-PBF Ti-6Al-4V have been revealed in the literature [13,17]. During the solidification process, columnar β grains are initially formed due to the steep thermal gradients in the melt pool. From above the β transus temperature, β grains are decomposed into α' martensitic laths resulting from the rapid cooling rate (10^4 – 10^6 K/s). L-PBF Ti-6Al-4V is often heat treated to relieve the residual stress, which coarsens the microstructure and transforms the α' martensite into α laths. Furthermore, the complex laser–matter interaction can trigger many metallurgical defects including surface roughness, porosity, and cracking [1,2]. Owing to the overwhelming resistance to crack formation of Ti-6Al-4V [18,19], only surface roughness and porosity are considered in our study. A combination of microstructure and process-induced defects govern the fatigue properties of the final product [13,14]. Hence, we need to focus on these aspects in this work.

The size-dependent fatigue behaviour of conventionally manufactured metallic material has been reported previously in the literature [20,21]. It is well-known that as the sample size increases, there is an increasing probability of encountering a larger defect thus provoking macroscopic failure [20,22]. But does this general principle hold for materials made by AM? Several reports have demonstrated the fatigue performance of net-shape AM Ti-6Al-4V is relatively inferior as compared to the conventionally manufactured counterpart — due to the presence of surface defects and porosity [13,14,22,23]. This may result

* Corresponding author.
E-mail address: jieming.zhang@queens.ox.ac.uk (J.S. Zhang).

https://doi.org/10.1016/j.addma.2023.103922
Received 6 July 2023; Received in revised form 25 October 2023; Accepted 11 December 2023
Available online 12 December 2023

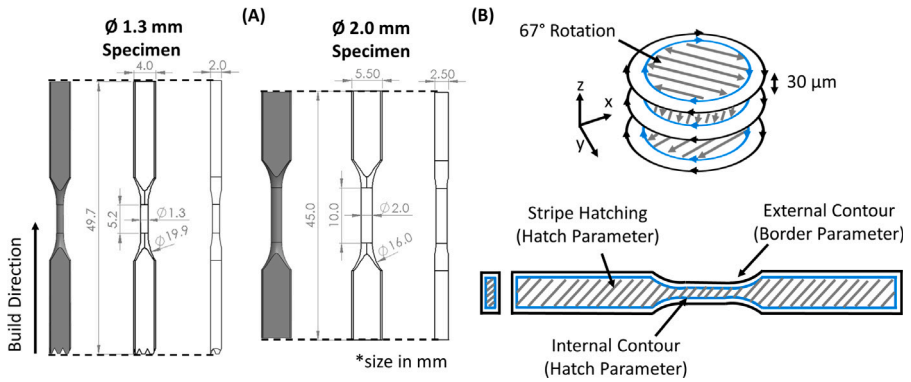

Fig. 1. (A) Geometries of the 2 tensile specimens used in this study. (B) Schematic illustrations of laser path along different consecutive layers and laser path along each cross-sectional plane.

Table 1
A summary of dimensions of samples used in this study.

Samples	Gauge diameter	Gauge length	Gauge length-to-diameter ratio
A	1.3 mm	5.2 mm	4
B	2 mm	10 mm	5

in a potentially different size effect phenomenon. An improvement in fatigue life has been found as the sample size increases owing to the enhanced surface quality [24–26]. However, the size-dependent fatigue behaviour of AM materials has not been researched yet in sufficient depth. The interplay between surface defects, porosity, and microstructure during the fatigue fracture process is still not clear. Furthermore, very little research has been found on the fatigue scatter — one of the key requirements to consider for the implementation of many applications.

With this in mind, we designed and fabricated net-shape AM specimens of different sizes to assess them in service conditions. The sample sizes chosen in this work correspond to the thicknesses of many engineering components, such as biomedical implants and heat exchangers. We performed uniaxial tensile tests to determine their quasi-static mechanical behaviour. We addressed the fatigue properties – fatigue life and fatigue scatter – as a function of the sample size. We focused particularly on their performance between 10^4 and 10^6 cycles to provide fundamental insight into the cyclic deformation behaviour of intricate component, especially metallic lattice. We revealed the microstructural features – grain size and texture – using high-resolution electron microscopy. The surface roughness and processing-induced porosity were quantified using X-ray computed tomography, which provides structural information of the specimens in three dimensions [7,27,28]. We analysed the fracture surfaces to understand the fatigue fracture process. Rationalization of our findings sheds light on how best to mitigate any structural inhomogeneity arising from the AM process.

2. Methods

2.1. Design of experimentation

To study the effect of sample size on the fatigue properties, specimens with two gauge diameters were considered: ∅ 1.3 mm and ∅ 2.0 mm — see Table 1. The two sample geometries are detailed in Fig. 1(A). A summary of sample dimensions is provided in Table 1. The difference in gauge length-to-diameter ratio between the two specimens is expected to only influence the calculated fracture strain but has minimal effect on the elastic modulus, yield strength, and ultimate tensile strength [29]. Owing to the larger gauge length-to-diameter ratio, the ∅ 2 mm specimen is expected to have a smaller fracture strain as compared to the ∅ 1.3 mm specimen after necking.

Table 2
Processing parameters used for the manufacturing of tensile samples.

Ti-6Al-4V	Hatch parameters	Border parameters
Layer thickness	30 µm	30 µm
Laser power	200 W	100 W
Laser scan speed	0.786 m/s	0.750 m/s
Point distance	55 µm	45 µm
Hatch distance	65 µm	65 µm
Exposure time	50 µs	40 µs
Spot size (Radius)	35 µm	35 µm

2.2. Processing by laser powder bed fusion

Tensile samples were produced using a Renishaw AM400 machine with a modulated 200 W ytterbium fibre laser. The powder fed into the machine was electrode induction-melted gas atomized Ti-6Al-4V provided by Renishaw plc. The processing parameters used are detailed in Table 2. A stripe hatching laser scan path pattern was employed with the path frame of reference being rotated by 67° after each layer was added (Fig. 1(B)). To achieve an optimal surface finish, two contour passes were performed near the free surfaces after each layer — the internal one using hatch parameters and the external one using border parameters (Fig. 1(C)). All samples were fabricated on a single build plate. The samples were stress relieved at 800 °C for 4 h in a vacuum furnace and sandblasted using safti grit at 2 bar. The post-processing was employed to examine the samples in the service conditions.

2.3. Assessment of static & dynamic mechanical behaviour

An Instron ElectroPuls E10k system with a 10 kN load cell was employed to measure the mechanical properties of the samples at room temperature. Uniaxial tensile tests were performed under displacement rate control at a strain rate of 2×10^{-3} s^{-1}. A non-contact iMetrum video extensometry system was used to measure the macroscopic strain of the sample on a 5.2 mm or a 10 mm gauge length.

Tensile fatigue tests were conducted under load control at a frequency of 30 Hz and an R ratio of 0.1. Maximum stresses of 600, 500 and 400 MPa were applied. At each applied stress, three tests were repeated. All samples were tested until fracture.

2.4. Characterization by electron microscopy

The microstructures were examined by a Zeiss Merlin field emission gun scanning electron microscope (FEG-SEM) equipped with a Bruker electron backscatter diffraction (EBSD) detector. Scans were performed on surfaces parallel to the build direction. The beam was operated at a 20 kV accelerating voltage and a 20 nA current. For the analysis of α lath thickness distribution, the diffraction patterns were collected

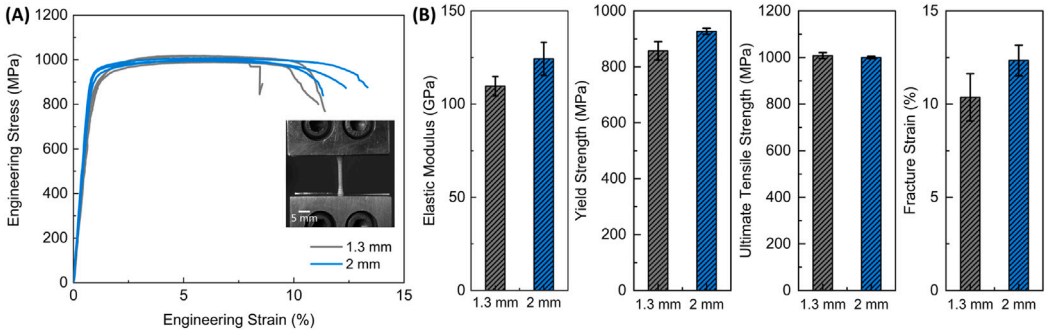

Fig. 2. (A) Engineering stress–strain curves of AM Ti-6Al-4V at a strain rate of 2×10^{-3} s^{-1}. (B) Elastic modulus, yield strength, ultimate tensile strength, and fracture strain of the 2 specimens under study. Error bars represent the standard deviation from 3 repetitions.

at 400 × 300 resolution with a step size of 0.22 μm. For the α lath texture analysis and the reconstruction of prior-β grains, the diffraction patterns were stored at 400 × 300 resolution with a step size of 0.55 μm.

Fractography was performed to examine the fracture behaviour of samples after fatigue tests using a JEOL 6500F FEG-SEM. The locations at which fatigue cracks initiate were identified to investigate the failure mechanisms.

2.5. X-ray Computed Tomography (XCT)

X-ray computed tomography of the tensile samples was carried out with an ImageiX CT system (North Star Imaging Inc., Minnesota, USA). During the measurement, each sample was placed 25.5 mm in front of the tungsten transmission target X-ray source filtered by a Cu foil of 0.95 mm thickness. Scans were performed at 140 kV tube voltage, 71 μA tube current, 5 μm focal spot size and 1 Hz frame rate. The isotropic voxel size was 4.7 μm - any feature smaller than 14.1 μm was deemed unresolvable [30]. Projection images were reconstructed using a filtered back Projection algorithm in the efX-ct software (version 1.9.5.12, North Star Imaging Inc., Minnesota, USA). Avizo 9.7 software was used to analyse the data. Solid parts were segmented using Otsu's method [31].

3. Results

3.1. Quasi-static behaviour

The quasi-static mechanical response of samples with different sizes is illustrated in Fig. 2(A). The tests were conducted following ASTM E8 standards [29]. The values of elastic modulus, yield strength, ultimate tensile strength, and fracture strain are summarized in Fig. 2(B). The ∅ 2 mm specimens demonstrate on average 14 GPa higher elastic modulus, 70 MPa higher yield strength, and 2% larger fracture strain but similar ultimate tensile strength as compared to the ∅ 1.3 mm specimens. A smaller fracture strain associated with the larger gauge length-to-diameter ratio samples is not observed. Instead, other factors are contributing to the larger fracture strain of the sample with the larger gauge length-to-diameter ratio. The fracture strain of the larger specimen would be even higher if the two specimens were of the same sample geometry. This size dependency is rationalized in Section 4.1.

3.2. Dynamic behaviour in fatigue

The fatigue performance of the 2 specimens is presented in Fig. 3(A). At all applied stresses, the larger specimens exhibit higher average cycles to failure than the smaller specimens. The differences in average cycles to failure increase as the maximum applied stress (σ_{max}) decreases. When σ_{max} = 600 MPa, the ∅ 2 mm specimen only demonstrates 11% higher average cycles to failure than the ∅ 1.3 mm specimen, and the differences become 27% and 130% at σ_{max} values of 500 MPa and 400 MPa, respectively.

To quantify the scatter in fatigue life at each applied stress, the coefficient of variation is used, defined as [32]:

$$\text{Coefficient of Variation} = \frac{\text{Standard Deviation}}{\text{Mean}} \quad (1)$$

Results are shown in Fig. 3(B). At all applied stresses, the ∅ 2 mm specimen demonstrates higher fatigue scatter as compared to the ∅ 1.3 mm specimen. Similar to the average cycles to failure, the difference in scatter in fatigue life also increases as the maximum applied stress decreases. At σ_{max} = 600 MPa, the larger specimen exhibits 6% higher scatter in fatigue life than the smaller specimen, and the difference becomes 17% and 30% at σ_{max} equal to 500 MPa and 400 MPa, respectively. The variation in fatigue properties between the 2 specimens is analysed in Section 4.3.

3.3. Microstructural characterization

The microstructural differences between the 2 specimens inherited from the AM process might also contribute to variations in fatigue properties. In our specimens, the microstructure consists of more than 95% of thin α laths organized in bundles within the prior-β grains. These grains are usually elongated parallel to the build direction. The size and texture of α laths and prior-β grains have been found to be strongly correlated with the fatigue properties of AM parts [33]. Hence, we describe the change in microstructure as a function of the sample size in this section by means of EBSD statistical analysis. In addition, we examine the microstructural features in the middle and edge sections of each specimen separately owing to the different processing parameters employed in these regions (Fig. 4(A)). The edge section is defined as 200 μm away from the sample surface based on the width of the two contour passes.

3.3.1. α lath microstructure

Fig. 4(B–E) presents the EBSD images of the 2 specimens under study. The α lath microstructure is clearly revealed. The thickness distribution of the α lath was measured by fitting an ellipse to each grain. The thickness of the lath was evaluated by the length of the short axis of the ellipse. More than 1500 α laths were analysed to obtain a statistical distribution for each sample. A summary of the results is shown in Fig. 4(F). The lath thickness in the ∅ 2 mm specimen is larger than that in the ∅ 1.3 mm specimen. This coarser microstructure can be related to the higher thermal mass of the larger samples. When larger samples are fabricated, they retain more heat and their average temperatures are higher than the smaller ones. This results in slower cooling rates and faster kinetics of martensitic decomposition [27,34,35].

Fig. 5(A) shows the EBSD map of the α lath microstructure at a lower magnification. The contour pole figure quantifies the texture strength for the three plane families {0001} $\{\bar{1}100\}$ and $\{\bar{1}2\bar{1}0\}$ with respect to the x–y plane of the sample. Among them, {0001} exhibits the

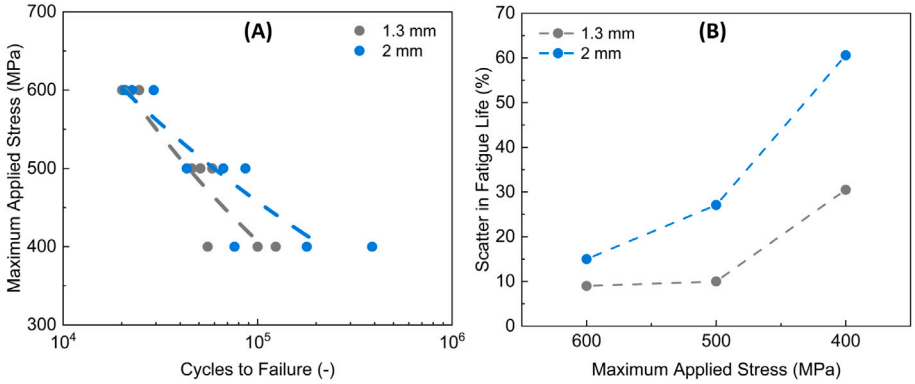

Fig. 3. (A) Maximum applied stress vs. cycles to failure for the specimens manufactured in this work. Three measurements are performed per condition. (B) Correlation between scatter in fatigue life and maximum applied stress for different tested specimens.

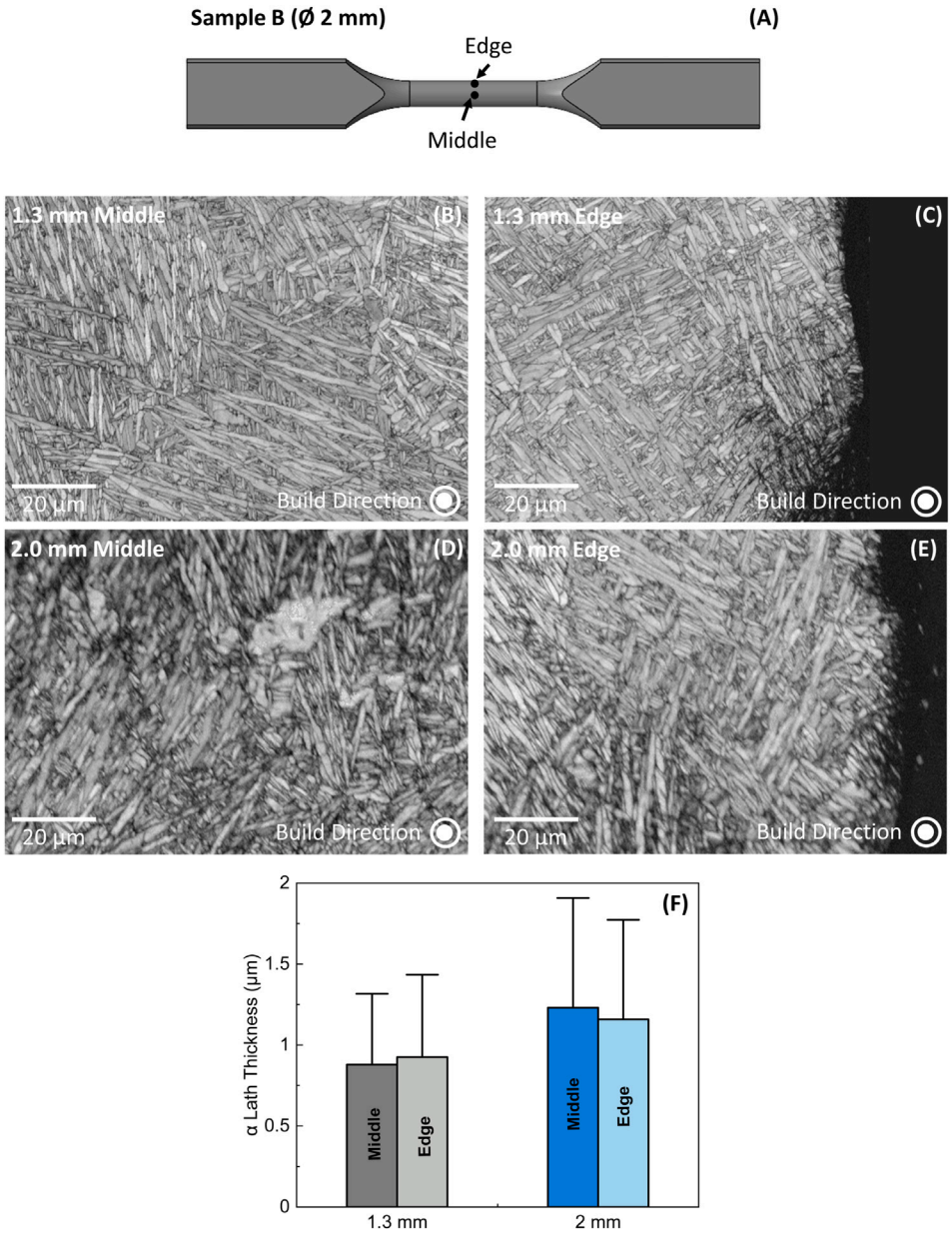

Fig. 4. (A) Schematic illustration of the positions at which the microstructural characterizations are performed in this work. (B–E) Cross sectional microstructure of the 2 specimens under study. (F) Average α lath thickness ±1 standard deviation of the 2 specimens.

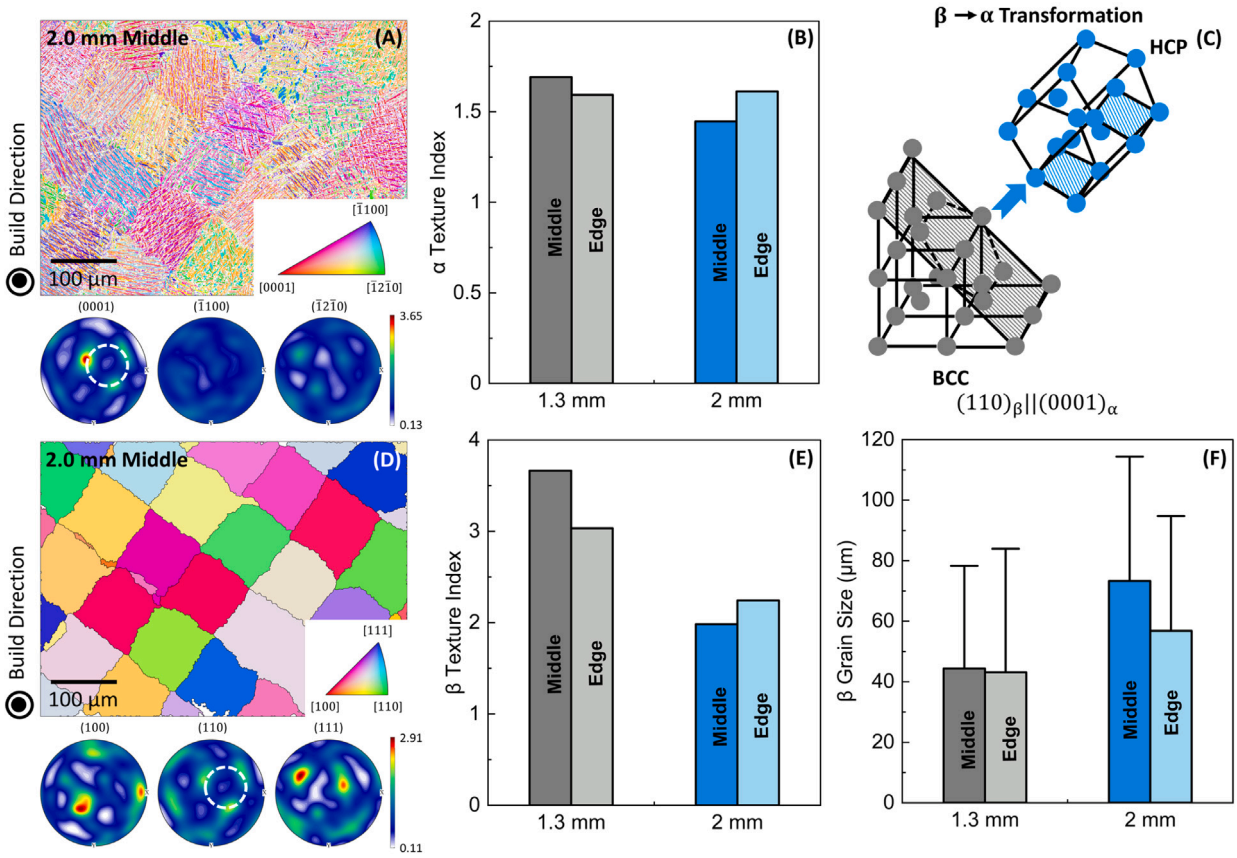

Fig. 5. (A) Cross sectional EBSD map and orientation distribution function pole figure of the α lath microstructure of the ∅ 2.0 mm sample. (B) Texture index of the α lath microstructure of the 2 specimens under study. (C) Schematic illustration of $\beta \rightarrow \alpha$ transformation during the AM process of Ti-6Al-4V. (D) Cross sectional EBSD map and orientation distribution function pole figure of the reconstructed prior-β microstructure of the ∅ 2.0 mm sample. (E) Texture index and (F) grain size of the reconstructed prior-β microstructure of the 2 specimens.

strongest texture, and it is parallel to the build direction. To compare the texture strength of different specimens, their α texture indices were evaluated as shown in Fig. 5(B) [36]. There is no significant difference in the texture of the α lath microstructure between the 2 specimens under study and the variation between the middle and edge sections of each specimen is also negligible.

3.3.2. Cross sectional prior-β grain microstructure

The prior-β grains are reconstructed from the descendant α lath structure using the MTEX 5.8.2 tool box following the transformation indicated in Fig. 5(C) [37]. In this method, each α lath is analysed together with the surrounding α laths to isolate the suitable prior-β grain based on the following Burgers orientation relationship [7]:

$$(110)_\beta//(0001)_\alpha, [111]_\beta//[11\bar{2}0]_\alpha \quad (2)$$

When the surrounding laths are of the same prior-β orientation, these laths are associated with the same prior-β grain. The procedure is iterated across the whole set of laths.

Fig. 5(D) presents the cross sectional EBSD map of the reconstructed prior-β grain. A grid plan pattern is observed in the middle section resulting from the 67° rotation of the stripe hatching scan between successive layers. On the other hand, irregular grains are formed in the edge section due to the contour scan. The texture strength for the three plane families {100} {110} and {111} with respect to the x–y plane of the sample is shown in the contour pole figure. In the ∅ 1.3 mm specimen, the (100) texture component is the strongest among the three whereas both the (100) and (111) exhibit similar texture strength in the ∅ 2 mm specimen. A transfer of texture between prior-β and α phases resulting from the crystallographic nature of the transformation can also be observed. The Burgers orientation relationship between the 2 phases – $(110)_\beta//(0001)_\alpha$ – is revealed in the pole figures corresponding to these directions. The texture ring along the $(110)_\beta$ is also observed along the $(0001)_\alpha$. This confirms the success of our reconstruction.

The prior-β texture indices of the 2 specimens are shown in Fig. 5(E) [36]. The ∅ 2 mm specimen demonstrates a 36% weaker texture as compared to the ∅ 1.3 mm specimen. The higher average temperatures within the larger specimen may give rise to a smaller thermal gradient, leading to fewer grains growing along the same direction [38,39]. However, such a variation in texture is not preserved during the martensitic transformation. The displacive phase transformation weakens the variant selection in Ti-6Al-4V alloys resulting in a weakly textured α lath microstructure [40–42]. In addition, the difference in texture between the middle and edge sections is not significant.

The sizes of the prior-β grains are measured for the 2 specimens. Results are shown in Fig. 5(F). Similar to our measurements on the α lath thickness, the ∅ 2 mm specimen exhibits larger prior-β grains than the ∅ 1.3 mm specimen, which results from the slower cooling rate during the manufacturing process. The coarser prior-β grains provide smaller numbers of α lath nucleation sites, which hinders nucleation and promotes propagation [43]. No significant difference in prior-β grain size can be found between the middle and edge sections of each specimen.

3.3.3. Longitudinal prior-β grain microstructure

The microstructure along the longitudinal plane is presented in Fig. 6(A) and (B). All the specimens show columnar grains along the build direction. The contour pole figure confirms (100) is the strongest texture component in the smaller specimen while (100) and (111) are

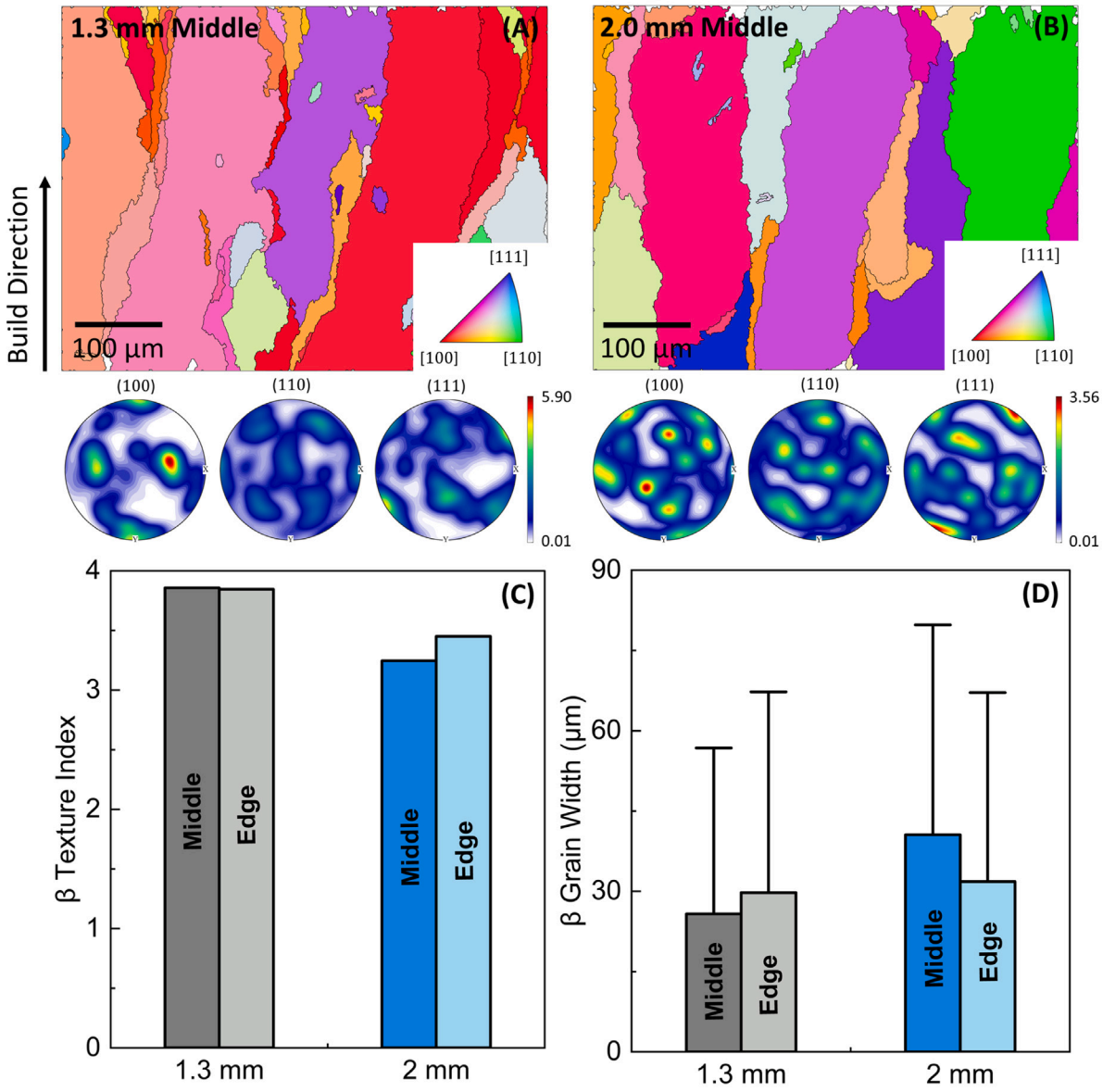

Fig. 6. Longitudinal EBSD map and orientation distribution function pole figure of the reconstructed prior-β microstructure of the (A) ∅ 1.3 mm sample and (B) ∅ 2.0 mm sample. (C) Texture index and (D) grain size of the reconstructed prior-β microstructure of the 2 samples.

equally strong in the larger specimen. The texture indices and grain widths extracted from these maps are shown in Fig. 6(C) and (D). The larger specimen demonstrates a weaker texture and larger columnar grain widths as compared to the smaller specimen, which is in agreement with the cross sectional microstructure.

3.4. Surface roughness

The surface quality of the 2 specimens was measured by comparing the XCT data with the CAD design. The XCT data is spatially registered with the CAD design by first aligning their centre of mass and principle axes as well as maximizing their mutual volume through translation and rotation. The distances between their surfaces are computed based on the closest points from the tomography data to the CAD design. As shown in Fig. 7(A), the red region represents the hills above the CAD design surface and the blue region represents the troughs below the surface. The surface roughness (R_a) is evaluated by integration over the entire profile x of length l, which can be given by [7]

$$R_a = \frac{1}{l}\int_0^l |h(x)|dx \tag{3}$$

where $h(x)$ is the relative height of the profile. Results are shown in Fig. 7(B). The surface roughness of the ∅ 2 mm specimen is only around 50% of that of the ∅ 1.3 mm specimen. This may be explained by the higher melt pool stability in the ∅ 2 mm specimen [2,44,45]. The higher temperature within the larger specimen enables powder particles to be melted more completely, minimizing balling effect.

3.5. Processing-induced porosity

The porosity of different samples is evaluated using the XCT data (Fig. 8(A)). Spatial distributions of the pores in the x–y plane of the 2 specimens are shown in Fig. 8(B). In both cases, porosity occurs largely

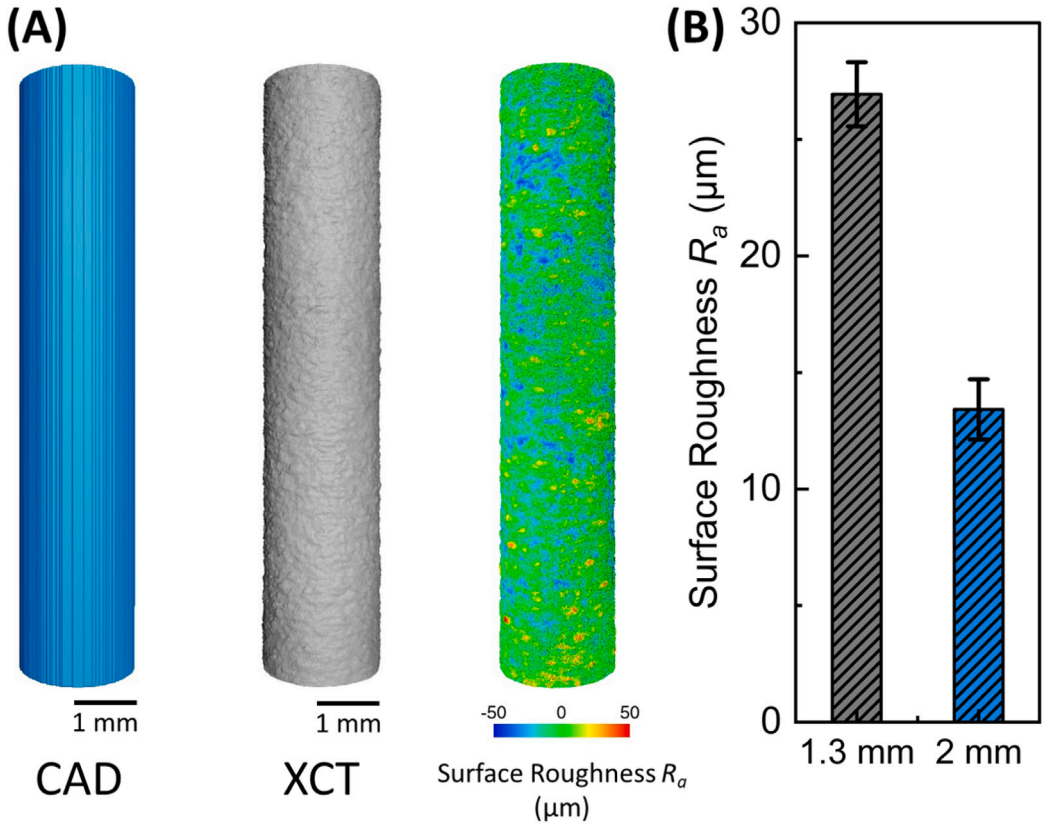

Fig. 7. (A) An example of the comparison between CAD design and computed tomography data. Red regions represent hills and blue regions represent pits. (B) Surface roughness (R_a) of the 2 specimens under study. Error bars represent the standard deviation from 3 repetitions. (For interpretation of the references to colour in this figure legend, the reader is referred to the web version of this article.)

near the sample surfaces. This statement is further supported by the quantification in Fig. 8(C). Nearly all the pores are found to be within 0.4 mm of the sample surfaces. Such a spatial dependency results from the mismatch between the stripe hatching and contour scan patterns and the gaps between contour passes [46–48].

The size and number density of the pores are also critical to the fatigue performance of AM component [49,50]. The size of the pores is characterized by the Murakami parameter $\sqrt{A_p}$ where A_p is the projection area, and their number density is given by the number of pores per unit volume [21,49]. Results are shown in Fig. 8(D). The ∅ 2 mm specimen exhibits a larger maximum pore size and higher number of pores per unit volume than the ∅ 1.3 mm specimen. This can be explained by the classical size effect phenomenon [20,32]. As the sample volume becomes larger, there is an increase in probability of encountering a large defect.

In addition, pore morphology is another important factor to consider. Irregular pores can be detrimental to the mechanical performance of the metallic part since a large stress concentration can be induced at the tips of sharp pore edges [51]. Hence, the irregularity of the pore is evaluated by the sphericity (Ψ) — a measure of how much the shape of the object deviates from a perfect sphere ($\Psi = 1$), which is given by [23]:

$$\Psi = \frac{\pi^{\frac{1}{3}}(6V_P)^{\frac{2}{3}}}{S_P} \tag{4}$$

where V_P is the pore volume and S_P is the surface area of the pore. The correlation between the sphericity and the equivalent diameter of the pore is present in Fig. 8(E). In both specimens, as the pores become larger, they tend to be more irregular.

Based on the value of the sphericity, we classify the pores into two categories: gas pores and lack-of-fusion pores. Keyhole pores are not expected due to the processing conditions employed in this study [19]. Above a sphericity of 0.7, the pores are categorized as gas pores and below 0.7, they are considered as lack-of-fusion pores [52]. The orientation of the lack-of-fusion pores can strongly influence the mechanical performance of the component [53]. When these irregular pores orient perpendicular to the loading direction, they could potentially deteriorate the mechanical performance the most. This is further supported by the results in Fig. 8(F). Those perpendicularly-oriented pores also exhibit a larger maximum projection area $A_{p,\ max}$ relative to the loading direction, which suggests they can possibly be the most critical pores within the specimens.

4. Discussion

Through systematic mechanical testing and characterization, we have revealed and quantified the significant impact of sample size on the fatigue properties, surface roughness, processing-induced porosity, and microstructural development of AM Ti-6Al-4V. Nevertheless, the results presented as yet require further rationalization and deeper understanding can be gained via more detailed analysis.

4.1. Rationalization of the variation in tensile properties

- **Elastic modulus, yield strength, and ultimate tensile strength:** In AM parts, the presence of geometrical deviations and porosity decreases the minimal cross-sectional area leading to reductions in static strength [54,55]. The smaller average

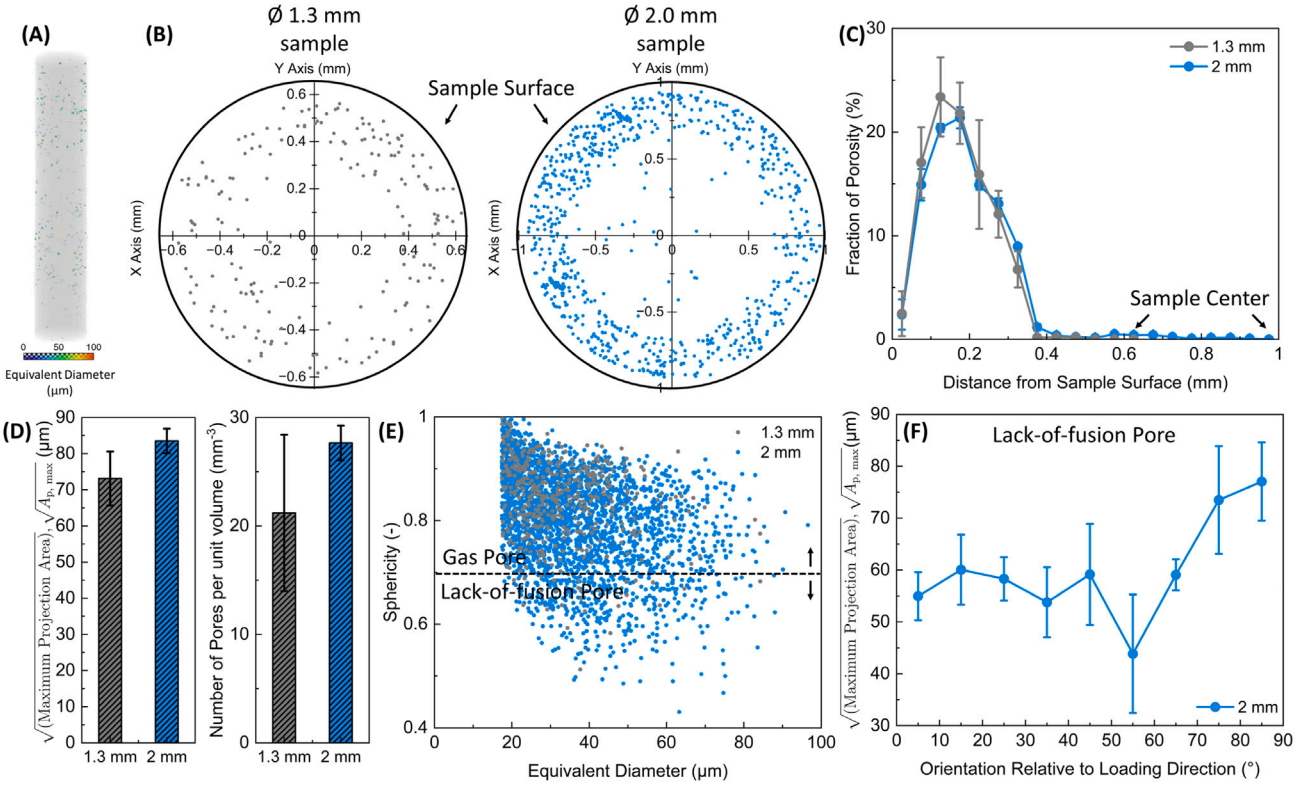

Fig. 8. (A) 3D rendered XCT images of a ∅ 2.0 mm sample and pores inside the sample. (B) Projection view of the porosity distribution along the build direction in the 2 specimens under study. (C) Fraction of porosity against the distance from sample surface. (D) $\sqrt{\text{Maximum Projection Area}}$, $\sqrt{A_{p,\,max}}$, and number of pores per unit volume of the 2 specimens. Error bars represent the standard deviation from 3 repetitions. (E) Sphericity vs. equivalent diameter of pores detected in this study. (F) $\sqrt{A_{p,\,max}}$ of lack-of-fusion pores as a function of the orientation relative to the loading direction.

cross-sectional area can also lower the measured elastic modulus. Here, we quantify the average and minimal cross-sectional area of the XCT data. The results are then normalized by the designed values as shown in Fig. 9(B). The larger specimen demonstrates around 5% higher proportions of both average and minimal cross-sectional areas than the smaller specimen, which indicates its results obtained from the engineering stress–strain curves are closer to the actual values.

If we take the average and minimal cross-sectional areas into account to correct the values of the elastic modulus and static strength separately, the differences in these properties between the two specimens become much smaller as shown in Fig. 9(C). Nevertheless, the ∅ 1.3 mm specimen still exhibits a 9 GPa lower elastic modulus than the ∅ 2 mm specimen, which can be attributed to the higher surface roughness of the smaller specimen. The surface irregularity can introduce plasticity into the sample even within the elastic region leading to an additional strain at a given stress [56].

On the other hand, the smaller specimen displays a comparable yield strength and an 80 MPa higher tensile strength than the larger specimen. Owing to the smaller α lath thickness in the ∅ 1.3 mm specimen, one would expect a higher yield strength (σ_y) following the Hall–Petch relationship [43]:

$$\sigma_y = \sigma_0 + \frac{k_y}{\sqrt{d}} \tag{5}$$

where σ_0 is a materials constant, k_y is a strengthening coefficient, and d is the α lath thickness. However, this might be diminished by the lower surface quality of the specimen [7]. Furthermore, the smaller lath thickness provides more grain boundaries for dislocations to pile up leading to higher work hardening and thus higher tensile strength [57].

- **Fracture strain:** The variation in fracture strain mainly results from two factors: surface roughness and microstructural difference. A significant reduction in surface quality of the smaller specimen gives more crack initiators resulting in premature failure [58]. Additionally, the finer microstructure can lead to lower crack tortuosity which facilitates the crack growth rate [59].

4.2. Fatigue fracture behaviour

Fig. 10(A) shows the morphology of the fracture surface of a fatigue tested sample. Clearly, three steps are involved in the fatigue fracture process. In region I, the cracks are initiated from surface defects. The surrounding regions are relatively flat, which indicates a slow growth rate. In region II, more grooves can be observed — which is representative of faster but steady crack growth. A zoomed-in view of this region displays the striation pattern formed by plastic blunting and sharpening of the crack tip under cyclic loading. Once the crack length reaches a certain threshold, the crack grows rapidly in an unstable manner. More details of the crack growth process can be found in Appendix. In region III, a dimpled fracture surface resulting from microvoid coalescence during the final failure can be observed.

The fatigue crack initiation sites for both types of specimens can be identified. In all the tested samples, the fatigue cracks initiate from the surface defects, which indicates surface quality is the most critical factor for the fatigue properties of the net-shape AM Ti-6Al-4V [60,61]. Such a surface initiated fracture process can be explained by linear elastic fracture mechanics. The stress intensity factor range (ΔK) for an arbitrarily shaped defect is given by [23]

$$\Delta K = Y \Delta\sigma \sqrt{\pi \sqrt{A_p}} \tag{6}$$

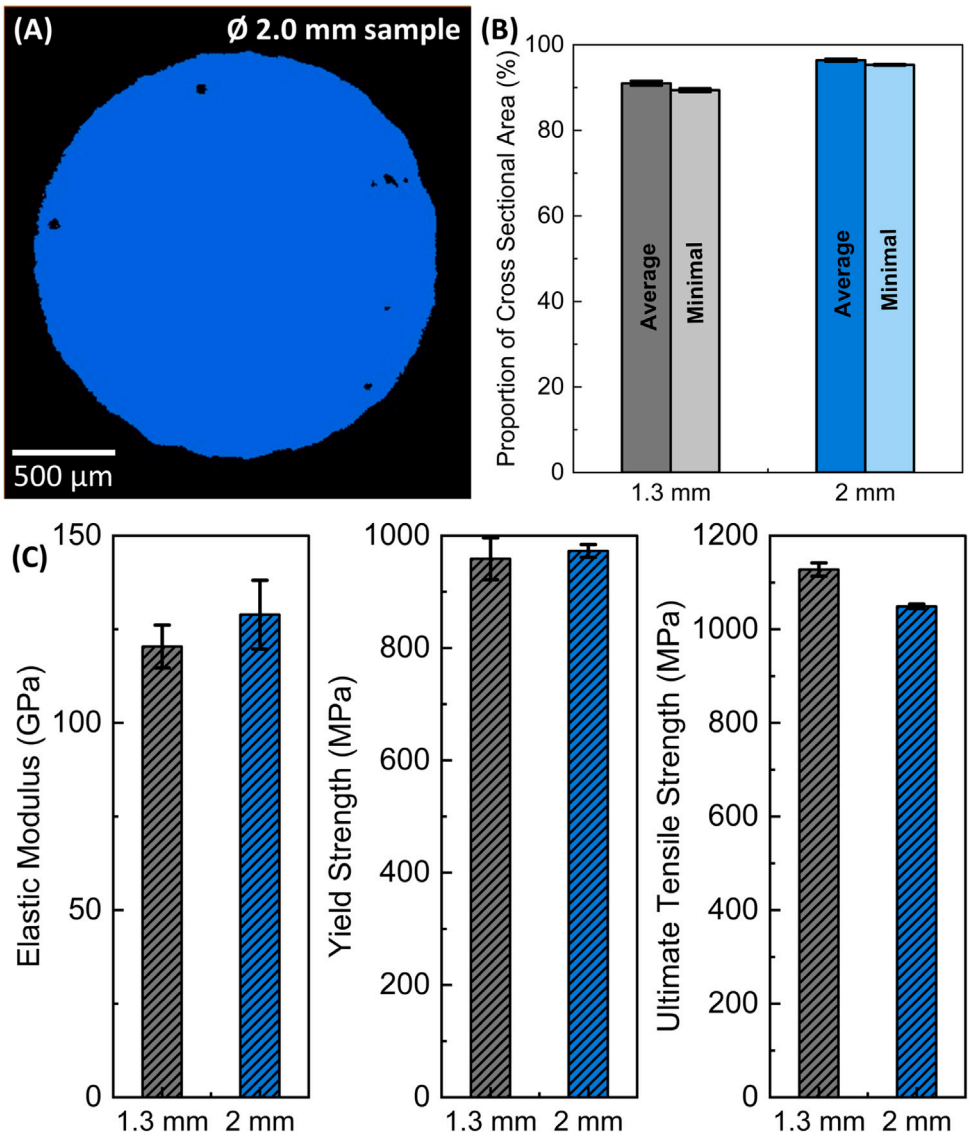

Fig. 9. (A) A segmented cross-sectional XCT slice of a ∅ 2.0 mm sample. (B) Proportions of average and minimal loading areas of the 2 specimens. (C) Corrected values of elastic modulus, yield strength, and ultimate tensile strength of the 2 specimens under study considering the effective loading area. Error bars represent the standard deviation from 3 specimens.

where Y is a geometrical factor, $\Delta\sigma$ is the range of the applied stress, and $\sqrt{A_p}$ is the square root of the projection area of a defect perpendicular to the load direction. The geometrical factor for an internal defect is 0.50 and that for a surface defect is 0.65 [62,63]. This means for defects of the same size, a surface defect can give rise to a higher stress intensity factor than an internal defect at the same applied stress. Hence, a surface defect is more likely to be the initiation site as compared to an internal defect.

In addition, some samples exhibit multiple fatigue crack initiation sites as shown in Fig. 10(B). However, no significant variation in cycles to failure has been found between these samples and those in which a single crack initiates. The probability of occurrence is also not vastly different between the two types of specimens. Several studies have reported that a pore cluster near the fatigue crack initiation site can increase the stress concentration and facilitate the initiation process [50,64]. Here, we account for a pore cluster near the initiation site when the distance between the pore and the initiation site is below 1 pore diameter. The effect of the pore on the local stress near the initiation site becomes negligible when they are further apart [50]. The probability of occurrence is no less than $\frac{1}{3}$ for both types of specimens, which indicates the influence of internal porosity on the fatigue fracture process cannot be neglected. No significant difference in contingency has been found between the two types of specimens in our study.

To understand the fracture behaviour quantitatively, we evaluate the striation spacing for all the tested samples. A zoomed-in view at a magnification of 10 000× is captured at the centre of region II for each tested sample. This is around 380 µm from the initiation site for the ∅ 1.3 mm specimen and 600 µm from the initiation site for the ∅ 2.0 mm specimen. The image intensity perpendicular to the striations is extracted using ImageJ and the striation spacing is determined by the distance between each peak as shown in Fig. 11(B). The spacing between 5 striations is analysed for each sample to ensure the repeatability of the result. Results are presented in Fig. 11(C). For both types of specimens, the fatigue striation spacing decreases as σ_{max} decreases. This can be explained by a slower crack growth rate ($\frac{da}{dN}$) induced by a lower stress intensity factor range (ΔK) following the

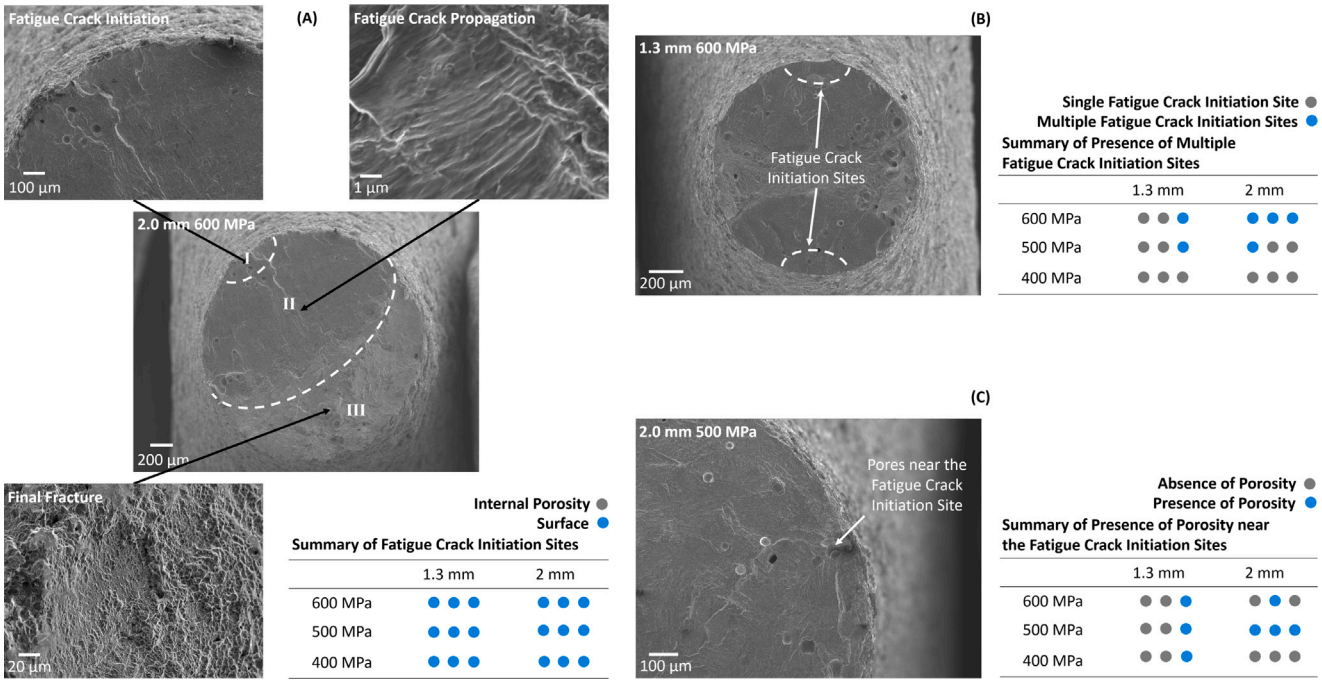

Fig. 10. Summary of fatigue fracture behaviours including (A) fatigue crack initiation sites, (B) presence of multiple fatigue crack initiation sites, and (C) presence of porosity near the fatigue crack initiation sites for all the tested samples.

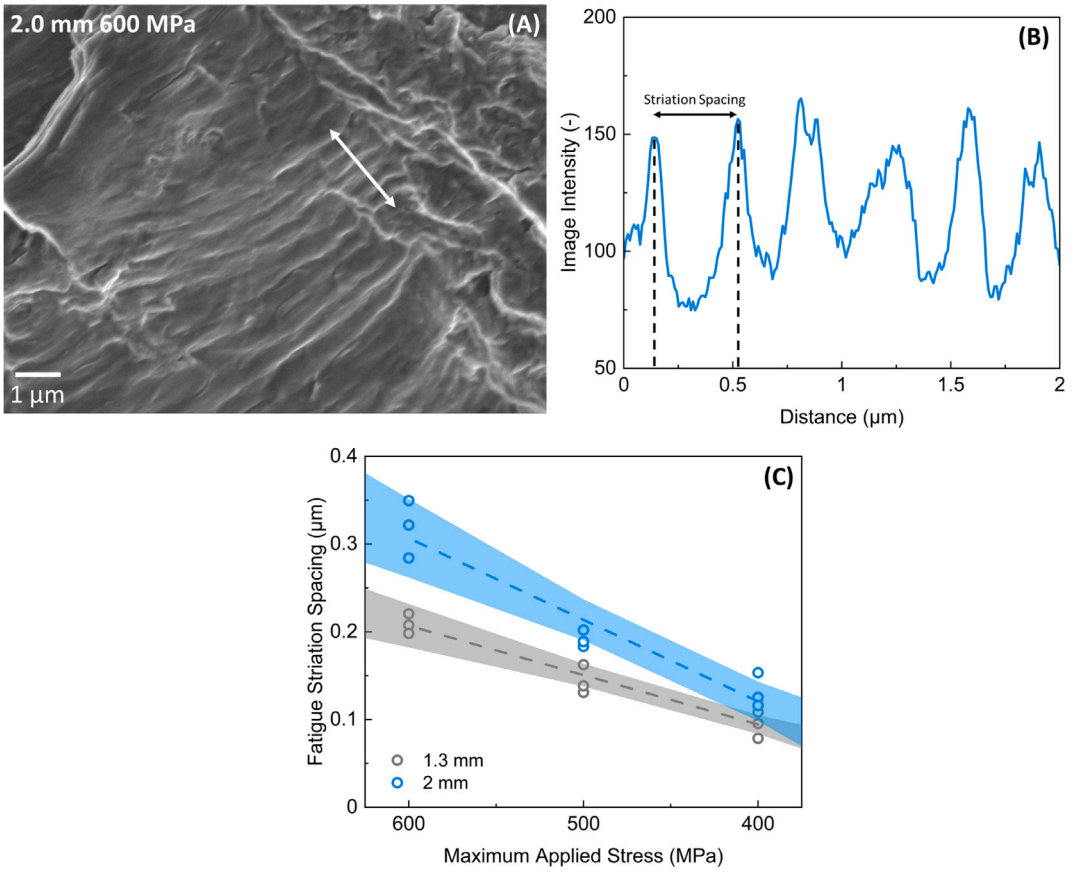

Fig. 11. (A) Fatigue striations observed on the fracture surface of a ∅ 2.0 mm sample tested at σ_{max} of 600 MPa. The arrow shows where the striation spacing analysis is performed. (B) Image intensity vs. distance along the arrow shown in (A). Striation spacing is characterized by the distance between the 2 peaks. (C) Correlation between fatigue striation spacing and maximum applied stress for the 2 specimens under study. Shaded area represents 95% confidence interval from 5 repetitions.

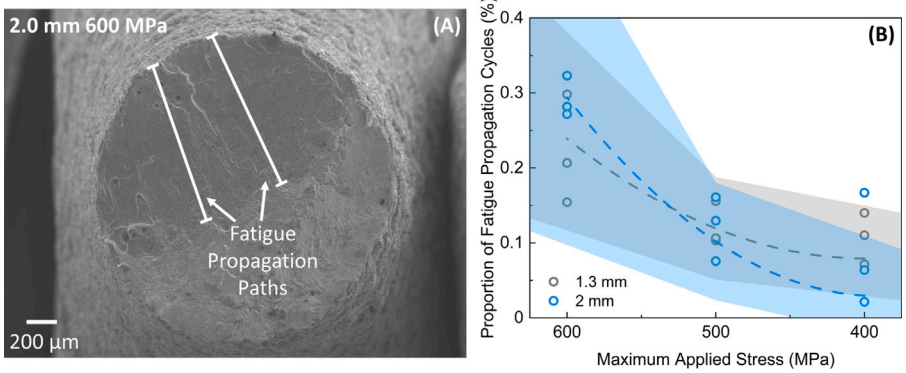

Fig. 12. (A) An example of the measurement of the length of fatigue propagation path. (B) Estimated proportion of fatigue propagation cycles as a function of the maximum applied stress. 95% confidence interval from 5 repetitions is shown in shaded area.

Paris' law [59]:

$$\frac{da}{dN} = C(\Delta K)^n \tag{7}$$

where C and n are materials constant. A lower incremental crack length gives rise to shorter striation spacing. Furthermore, the ∅ 2 mm specimen exhibits larger striation spacing than the ∅ 1.3 mm specimen at all applied stresses. This can be attributed to the different crack lengths of the observation locations in the two types of specimens. The observations were made at larger crack lengths for the larger specimens, which results in higher ΔK and thus larger incremental crack length.

Based on the evaluation of striation spacing, we estimate the proportion of the fatigue life during which the crack propagates for all the tested samples. The length of the fatigue propagation path is measured using ImageJ as shown in Fig. 12(A). For samples with multiple crack initiation sites, all propagation paths are considered. The number of cycles to propagate the crack across the specimen is then estimated by dividing the total propagation path length by the striation spacing at the centre of region II. This is then normalized by the cycles to failure to determine the proportion of the lifetime spent in the propagation stage. Results are shown in Fig. 12(B). The proportion of fatigue propagation cycle is lower than 40% for all the samples, which indicates crack propagation is not the dominant stage of the failure process and fatigue failure is eventually initiation process controlled. This confirms that our tests were performed in the high cycle fatigue regime [65–67]. Additionally, the proportion of fatigue life due to crack propagation decreases as σ_{max} decreases for both types of specimens. This implies the failure process becomes more initiation driven as the stress is decreased.

It is crucial to note that the approach described above does not provide an accurate evaluation of the fatigue propagation cycle but it gives a good estimation of the proportion of fatigue propagation during the entire fracture process. The results are valid to shed light on the fatigue fracture process and the trend in behaviour with σ_{max} would remain the same.

4.3. Rationalization of the variation in fatigue properties

On the basis of the results presented in Section 4.2, the difference in fatigue properties between the two types of specimens can be rationalized. The surface initiated fracture process at all applied stresses confirms the higher fatigue resistance of the ∅ 2 mm specimen is primarily due to the 50% lower surface roughness as compared to the ∅ 1.3 mm specimen. As σ_{max} decreases, the number of cycles required to initiate a crack from a surface defect becomes more dominant in determining the fatigue life, leading to a larger difference in the average number of cycles to failure.

Having surface defects as the initiation sites cannot completely eliminate the contribution of internal porosity to the fatigue fracture process. We have measured the $\sqrt{\text{Projection Area}}$, $\sqrt{A_p}$, of the pore cluster near the fatigue initiation site for each of the tested sample. Results are shown in Fig. 13. ○ is used to denote samples without a pore cluster near the initiation site. For both types of specimens, pore clusters can be found near the initiation site in samples with the lowest cycles to failure at each applied stress. This highlights that internal porosity can degrade the fatigue performance of AM Ti-6Al-4V even when the fatigue crack is initiated from a surface defect. It is noteworthy that only the interaction between surface defects and internal pores on the fracture surface has been assessed in this study. The coalescence with any pores below or above the surface cannot be detected, which may also facilitate the fatigue fracture process [68].

Furthermore, the internal porosity has been found to contribute more to the fatigue fracture process of the larger specimen than that of the smaller specimen for the following two reasons. (1) The 50% lower surface roughness of the larger specimen results in a smaller stress intensity factor range, which means a smaller contribution to the failure process from the surface defects. (2) A higher number density of pores with larger sizes have been found close to the sample surface in the larger specimen (Section 3.5), which potentially gives rise to a higher stress concentration. This has been confirmed by the fracture surface analysis.

The more significant contribution from the internal porosity to the fracture process in the larger specimen may explain the higher scatter in fatigue life, which can be associated with the larger variation in pore characteristics, primarily pore size, in these specimens [50]. As the stress is decreased, the precise location and orientation of the pore cluster can have a significant effect on the stress concentration at the initiation site and therefore the number of cycles to initiate a crack. Hence, initiation becomes sensitive to the proximity of the pore clusters, giving rise to increased scatter.

Finally, the microstructural differences between the two types of specimens cannot be totally discounted. Several studies have reported that a finer microstructure can give rise to a higher fatigue strength in the high cycle fatigue regime since a higher number of grain boundaries can impede the dislocation motion [14,69,70]. However, this is not in agreement with our results. Here, the presence of surface defects and internal porosity dominates the failure process. Nevertheless, the coarser microstructure of the larger specimen exhibits a stronger defect

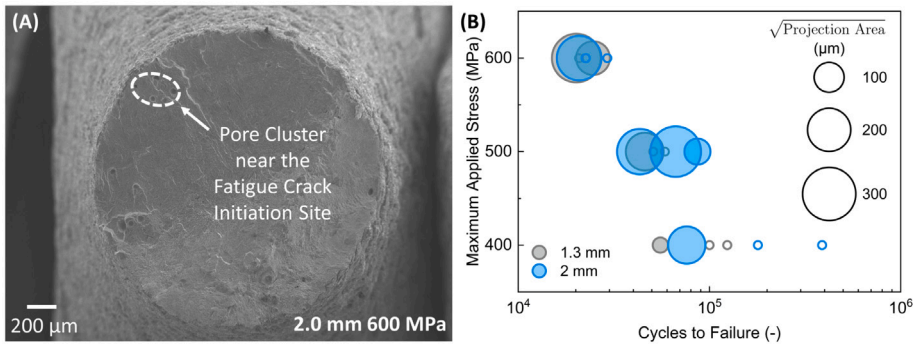

Fig. 13. (A) An example of the measurement of the projection area, A_p, of pore cluster near the fatigue crack initiation site. (B) $\sqrt{A_p}$ of the pore cluster for different tested specimens. ○ represents the specimens without pore cluster near the initiation site.

tolerance. A higher threshold for stress intensity factor range is needed to trigger the crack growth [13,14]. Additionally, thicker α laths tend to induce more corrugated crack paths, which provides a higher resistance to fatigue crack growth in the larger specimen [71,72].

5. Summary and conclusions

To study the effect of sample size, we have performed systematic mechanical testing, high-resolution electron microscopy, and X-ray computed tomography on L-PBF Ti-6Al-4V material to evaluate the variation in fatigue behaviour and how this is influenced by microstructure, surface quality, and processing-induced porosity. Two sample sizes have been considered: ∅ 1.3 mm and ∅ 2.0 mm. The following specific conclusions can be drawn from this work:

- The larger specimen exhibits superior fatigue life in the high cycle fatigue regime: at σ_{max} = 600 MPa, it is 11% greater; at σ_{max} = 500 MPa, it is 27% greater; at σ_{max} = 400 MPa, it is 130% greater. The scatter in fatigue life is approximately double that of the smaller specimen.
- Surface defects serve as the fatigue crack initiation sites for all the cases in this work. A reduction of surface roughness by 50% in the larger specimen contributes positively to the higher fatigue life. As σ_{max} decreases, the fracture process becomes more surface initiation-driven leading to larger differences in fatigue life between the two types of specimen.
- Clusters of pores have often been found near the crack initiation sites thus facilitating the fatigue initiation process. The larger contribution of porosity to the fatigue fracture process is likely to be contributing to the higher fatigue scatter exhibited by the larger specimens. At lower σ_{max}, the stress concentration from any pore cluster becomes a more dominant factor in determining the number of cycles for crack initiation.
- It seems that the different microstructure has only a minimal influence on the variation in fatigue behaviour observed. Nonetheless, the thicker α laths of the larger specimen can give rise to a higher tolerance to defects and more tortuous crack paths, which impedes fatigue crack growth.

CRediT authorship contribution statement

Jieming S. Zhang: Writing – original draft, Investigation, Conceptualization. **Yuanbo T. Tang:** Writing – review & editing, Investigation, Conceptualization. **Ruining Jin:** Investigation. **Andrew Lui:** Investigation. **Patrick S. Grant:** Writing – review & editing. **Enrique Alabort:** Funding acquisition. **Alan C.F. Cocks:** Writing – review & editing, Supervision. **Roger C. Reed:** Writing – review & editing, Funding acquisition.

Declaration of competing interest

The authors declare that they have no known competing financial interests or personal relationships that could have appeared to influence the work reported in this paper.

Data availability

Data will be made available on request.

Acknowledgements

Jieming S. Zhang would like to thank Prof. Andrew Horsfield and Prof. David Dye for their inspirations to start this DPhil study. Helpful comments from Prof. Marco Simonelli of University of Nottingham, Dr. Enzo Liotti, Dr. Yun Deng, Dr. Insung Han, Dr. Joseph N. Ghoussoub, and Prof. D. Graham McCartney of University of Oxford are acknowledged. The authors are grateful for the funding from Alloyed Ltd. and Innovate UK 43749. Yuanbo T. Tang and Roger C. Reed acknowledge support from the Henry Royce Institute for Advanced Materials, funded through EPSRC, United Kingdom grants (EP/R00661X/1) and (EP/X527257/1).

Appendix. Evolution of fatigue crack growth

To provide quantitative evidence of the fatigue crack growth process, we measure the variation in striation spacing during the fracture process. Zoomed-in views at four different locations are captured along the fatigue propagation path as shown in Fig. A.1(A). The spacing between 5 striations is analysed at each location. Results are shown in Fig. A.1(B). In both cases, almost no striations can be observed within a normalized distance of 0.3. Above 0.3, the striation spacing increases as the distance from the initiation site increases. This results from the higher ΔK at larger crack lengths leading to larger incremental crack lengths. Moreover, the striation spacing of the two types of specimens almost overlaps at the same distance from the initiation site, which confirms the crack growth behaviour can be described by Paris' law in Eq. (7). The deviation in the number of cycles to propagate the crack between the two types of specimens mainly results from the difference in the propagation length.

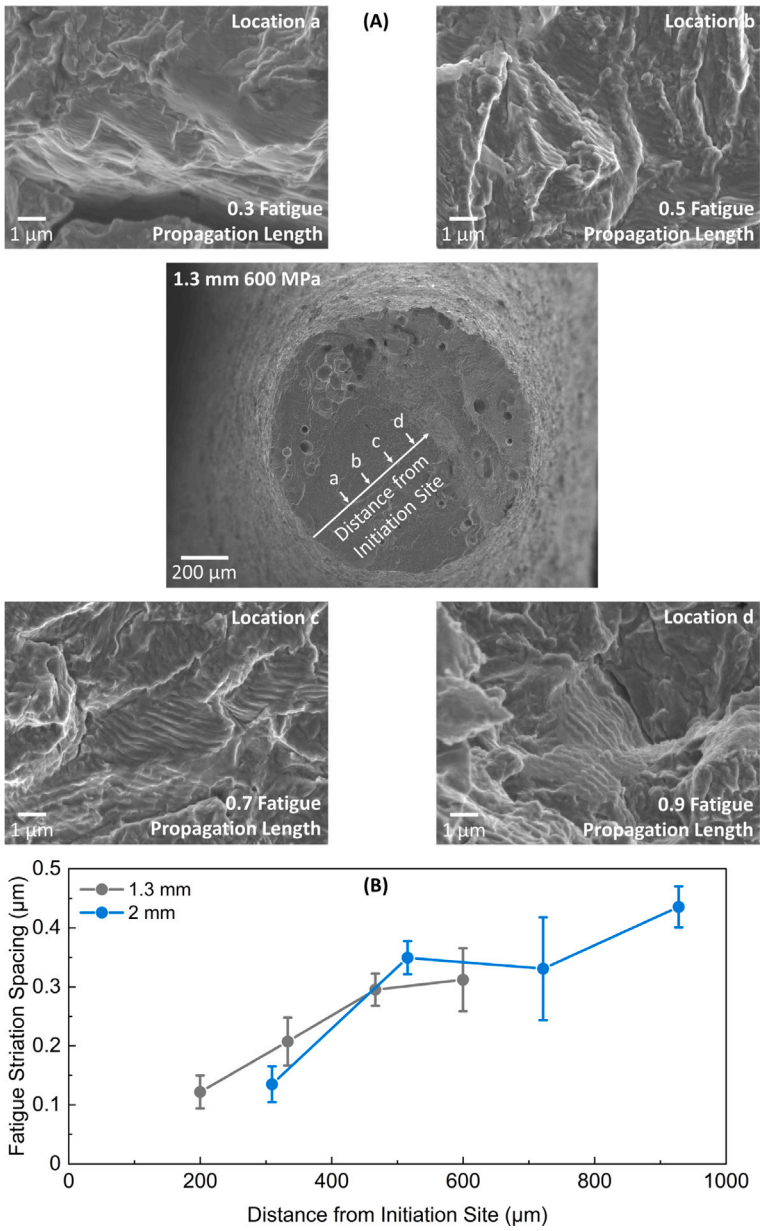

Fig. A.1. (A) An example of the measurement of the distance from the initiation site. (B) Correlation between fatigue striation spacing and distance from the initiation site for the 2 specimens tested at 600 MPa. Error bars represent the standard deviation from 5 repetitions.

References

[1] D. Gu, X. Shi, R. Poprawe, D.L. Bourell, R. Setchi, J. Zhu, Material-structure-performance integrated laser-metal additive manufacturing, Science 372 (6545) (2021) http://dx.doi.org/10.1126/science.abg1487.

[2] T. DebRoy, H.L. Wei, J.S. Zuback, T. Mukherjee, J.W. Elmer, J.O. Milewski, A.M. Beese, A. Wilson-Heid, A. De, W. Zhang, Additive manufacturing of metallic components – process, structure and properties, Prog. Mater. Sci. 92 (2018) 112–224, http://dx.doi.org/10.1016/j.pmatsci.2017.10.001.

[3] D. Barba, E. Alabort, R.C. Reed, Synthetic bone: Design by additive manufacturing, Acta Biomater. 97 (2019) 637–656, http://dx.doi.org/10.1016/j.actbio.2019.07.049.

[4] X. Zheng, H. Lee, T.H. Weisgraber, M. Shusteff, J. DeOtte, E.B. Duoss, J.D. Kuntz, M.M. Biener, Q. Ge, J.A. Jackson, S.O. Kucheyev, N.X. Fang, C.M. Spadaccini, Ultralight, ultrastiff mechanical metamaterials, Science 344 (6190) (2014) 1373–1377, http://dx.doi.org/10.1126/science.1252291.

[5] M.S. Pham, C. Liu, I. Todd, J. Lertthanasarn, Damage-tolerant architected materials inspired by crystal microstructure, Nature 565 (7739) (2019) 305–311, http://dx.doi.org/10.1038/s41586-018-0850-3.

[6] C.N. Kelly, J. Francovich, S. Julmi, D. Safranski, R.E. Guldberg, H.J. Maier, K. Gall, Fatigue behavior of as-built selective laser melted titanium scaffolds with sheet-based gyroid microarchitecture for bone tissue engineering, Acta Biomater. 94 (2019) 610–626, http://dx.doi.org/10.1016/j.actbio.2019.05.046.

[7] D. Barba, C. Alabort, Y.T. Tang, M.J. Viscasillas, R.C. Reed, E. Alabort, On the size and orientation effect in additive manufactured Ti-6Al-4V, Mater. Des. 186 (2020) 108235, http://dx.doi.org/10.1016/j.matdes.2019.108235.

[8] B.E. Carroll, T.A. Palmer, A.M. Beese, Anisotropic tensile behavior of Ti-6Al-4V components fabricated with directed energy deposition additive manufacturing, Acta Mater. 87 (2015) 309–320, http://dx.doi.org/10.1016/j.actamat.2014.12.054.

[9] B. Aksakal, Ö.S. Yildirim, H. Gul, Metallurgical failure analysis of various implant materials used in orthopedic applications, J. Fail. Anal. Prev. 4 (3) (2004) 17–23, http://dx.doi.org/10.1361/15477020419794.

[10] S. Romano, A. Brückner-Foit, A. Brandão, J. Gumpinger, T. Ghidini, S. Beretta, Fatigue properties of AlSi10Mg obtained by additive manufacturing: Defect-based modelling and prediction of fatigue strength, Eng. Fract. Mech. 187 (2018) 165–189, http://dx.doi.org/10.1016/j.engfracmech.2017.11.002.

[11] A. Yadollahi, N. Shamsaei, Additive manufacturing of fatigue resistant materials: Challenges and opportunities, Int. J. Fatigue 98 (2017) 14–31, http://dx.doi.org/10.1016/j.ijfatigue.2017.01.001.

[12] Z. Liu, B. He, T. Lyu, Y. Zou, A review on additive manufacturing of titanium alloys for aerospace applications: Directed energy deposition and beyond Ti-6Al-4V, JOM 73 (6) (2021) 1804–1818, http://dx.doi.org/10.1007/s11837-021-04670-6.

[13] Y. Zhai, H. Galarraga, D.A. Lados, Microstructure, static properties, and fatigue crack growth mechanisms in Ti-6Al-4V fabricated by additive manufacturing: LENS and EBM, Eng. Fail. Anal. 69 (2016) 3–14, http://dx.doi.org/10.1016/j.engfailanal.2016.05.036.

[14] S. Liu, Y.C. Shin, Additive manufacturing of Ti6Al4V alloy: A review, Mater. Des. 164 (2019) 107552, http://dx.doi.org/10.1016/j.matdes.2018.107552.

[15] M. McGregor, S. Patel, S. McLachlin, Mihaela Vlasea, Architectural bone parameters and the relationship to titanium lattice design for powder bed fusion additive manufacturing, Addit. Manuf. 47 (April) (2021) 102273, http://dx.doi.org/10.1016/j.addma.2021.102273, arXiv:2105.07945.

[16] A. Vafadar, F. Guzzomi, A. Rassau, K. Hayward, Advances in metal additive manufacturing: A review of common processes, industrial applications, and current challenges, Appl. Sci. (Switzerland) 11 (3) (2021) 1–33, http://dx.doi.org/10.3390/app11031213.

[17] L. Thijs, F. Verhaeghe, T. Craeghs, J.V. Humbeeck, J.P. Kruth, A study of the microstructural evolution during selective laser melting of Ti-6Al-4V, Acta Mater. 58 (9) (2010) 3303–3312, http://dx.doi.org/10.1016/j.actamat.2010.02.004.

[18] T. Mukherjee, J.S. Zuback, A. De, T. DebRoy, Printability of alloys for additive manufacturing, Sci. Rep. 6 (2016) 1–8, http://dx.doi.org/10.1038/srep19717.

[19] H. Gong, K. Rafi, H. Gu, T. Starr, B. Stucker, Analysis of defect generation in Ti-6Al-4V parts made using powder bed fusion additive manufacturing processes, Addit. Manuf. 1 (2014) 87–98, http://dx.doi.org/10.1016/j.addma.2014.08.002.

[20] A. Carpinteri, A. Spagnoli, S. Vantadori, Size effect in S-N curves: A fractal approach to finite-life fatigue strength, Int. J. Fatigue 31 (5) (2009) 927–933, http://dx.doi.org/10.1016/j.ijfatigue.2008.10.001.

[21] D. El Khoukhi, F. Morel, N. Saintier, D. Bellett, P. Osmond, V.D. Le, Probabilistic modeling of the size effect and scatter in high cycle fatigue using a Monte-Carlo approach: Role of the defect population in cast aluminum alloys, Int. J. Fatigue 147 (January) (2021) 106177, http://dx.doi.org/10.1016/j.ijfatigue.2021.106177.

[22] T. Tomaszewski, Modelling of critical defect distributions for estimating the size effect of selective laser melted 316l stainless steel, Int. J. Fatigue 167 (PA) (2023) 107378, http://dx.doi.org/10.1016/j.ijfatigue.2022.107378.

[23] T.H. Becker, P. Kumar, U. Ramamurty, Fracture and fatigue in additively manufactured metals, Acta Mater. 219 (2021) 117240, http://dx.doi.org/10.1016/j.actamat.2021.117240.

[24] J. Pegues, M. Roach, R. Scott Williamson, N. Shamsaei, Surface roughness effects on the fatigue strength of additively manufactured Ti-6Al-4V, Int. J. Fatigue 116 (April) (2018) 543–552, http://dx.doi.org/10.1016/j.ijfatigue.2018.07.013.

[25] S.M. Razavi, B. Van Hooreweder, F. Berto, Effect of build thickness and geometry on quasi-static and fatigue behavior of Ti-6Al-4V produced by electron beam melting, Addit. Manuf. 36 (November 2019) (2020) 101426, http://dx.doi.org/10.1016/j.addma.2020.101426.

[26] S. Ghods, R. Schur, A. Montelione, R. Schleusener, D.D. Arola, M. Ramulu, Importance of build design parameters to the fatigue strength of Ti6Al4V in electron beam melting additive manufacturing, Materials 15 (16) (2022) http://dx.doi.org/10.3390/ma15165617.

[27] Z. Dong, X. Zhang, W. Shi, H. Zhou, H. Lei, J. Liang, Study of size effect on microstructure and mechanical properties of AlSi10Mg samples made by selective laser melting, Materials 11 (12) (2018) http://dx.doi.org/10.3390/ma11122463.

[28] E. Hernández-Nava, C.J. Smith, F. Derguti, S. Tammas-Williams, F. Léonard, P.J. Withers, I. Todd, R. Goodall, The effect of density and feature size on mechanical properties of isostructural metallic foams produced by additive manufacturing, Acta Mater. 85 (2015) 387–395, http://dx.doi.org/10.1016/j.actamat.2014.10.058.

[29] ASTM E8, ASTM E8/E8M standard test methods for tension testing of metallic materials 1, Annu. Book ASTM Stand. 4 (C) (2010) 1–27, http://dx.doi.org/10.1520/E0008.

[30] E. Maire, P.J. Withers, E. Maire, P.J. Withers, Quantitative X-ray tomography, Int. Mater. Rev. 59 (1) (2014) 1–43, http://dx.doi.org/10.1179/1743280413Y.0000000023.

[31] N. Otsu, A threshold selection method from gray-level histograms, IEEE Trans. Syst. Man Cybern. 9 (1) (1979) 62–66.

[32] D. El Khoukhi, F. Morel, N. Saintier, D. Bellett, P. Osmond, V.D. Le, J. Adrien, Experimental investigation of the size effect in high cycle fatigue: Role of the defect population in cast aluminium alloys, Int. J. Fatigue 129 (May) (2019) 105222, http://dx.doi.org/10.1016/j.ijfatigue.2019.105222.

[33] J.W. Pegues, S. Shao, N. Shamsaei, N. Sanaei, A. Fatemi, D.H. Warner, P. Li, N. Phan, Fatigue of additive manufactured ti-6al-4v, part I: The effects of powder feedstock, manufacturing, and post-process conditions on the resulting microstructure and defects, Int. J. Fatigue 132 (November 2019) (2020) http://dx.doi.org/10.1016/j.ijfatigue.2019.105358.

[34] X. Tan, Y. Kok, Y.J. Tan, G. Vastola, Q.X. Pei, G. Zhang, Y.W. Zhang, S.B. Tor, K.F. Leong, C.K. Chua, An experimental and simulation study on build thickness dependent microstructure for electron beam melted Ti-6Al-4V, J. Alloys Compd. 646 (2015) 303–309, http://dx.doi.org/10.1016/j.jallcom.2015.05.178.

[35] N.T. Aboulkhair, N.M. Everitt, I. Ashcroft, C. Tuck, Reducing porosity in AlSi10Mg parts processed by selective laser melting, Addit. Manuf. 1 (2014) 77–86, http://dx.doi.org/10.1016/j.addma.2014.08.001.

[36] R. Hielscher, H. Schaeben, A novel pole figure inversion method: Specification of the mtex algorithm, J. Appl. Crystallogr. 41 (6) (2008) 1024–1037, http://dx.doi.org/10.1107/S0021889808030112.

[37] C. Leyens, M. Peters, Titanium and Titanium Alloys, 2003, http://dx.doi.org/10.1007/978-3-319-69743-7_7.

[38] N. Raghavan, R. Dehoff, S. Pannala, S. Simunovic, M. Kirka, J. Turner, N. Carlson, S.S. Babu, Numerical modeling of heat-transfer and the influence of process parameters on tailoring the grain morphology of IN718 in electron beam additive manufacturing, Acta Mater. 112 (2016) 303–314, http://dx.doi.org/10.1016/j.actamat.2016.03.063.

[39] Y. Wang, C. Yu, L. Xing, K. Li, J. Chen, W. Liu, J. Ma, Z. Shen, Grain structure and texture of the SLM single track, J. Mater Process. Technol. 281 (November 2019) (2020) 116591, http://dx.doi.org/10.1016/j.jmatprotec.2020.116591.

[40] H. Beladi, Q. Chao, G.S. Rohrer, Variant selection and intervariant crystallographic planes distribution in martensite in a Ti-6Al-4V alloy, Acta Mater. 80 (2014) 478–489, http://dx.doi.org/10.1016/j.actamat.2014.06.064.

[41] K. Yamanaka, W. Saito, M. Mori, H. Matsumoto, A. Chiba, Preparation of weak-textured commercially pure titanium by electron beam melting, Addit. Manuf. 8 (2015) 105–109, http://dx.doi.org/10.1016/j.addma.2015.09.007.

[42] X.P. Li, J. Van Humbeeck, J.P. Kruth, Selective laser melting of weak-textured commercially pure titanium with high strength and ductility: A study from laser power perspective, Mater. Des. 116 (2017) 352–358, http://dx.doi.org/10.1016/j.matdes.2016.12.019.

[43] I. Ghamarian, B. Hayes, P. Samimi, B.A. Welk, H.L. Fraser, P.C. Collins, Developing a phenomenological equation to predict yield strength from composition and microstructure in β processed Ti-6Al-4V, Mater. Sci. Eng. A 660 (2016) 172–180, http://dx.doi.org/10.1016/j.msea.2016.02.052.

[44] K. Kempen, B. Vrancken, S. Buls, L. Thijs, J. Van Humbeeck, J.P. Kruth, Selective laser melting of crack-free high density M2 high speed steel parts by baseplate preheating, Trans. ASME, J. Manuf. Sci. Eng. 136 (6) (2014) 1–6, http://dx.doi.org/10.1115/1.4028513.

[45] O. Poncelet, M. Marteleur, C. van der Rest, O. Rigo, J. Adrien, S. Dancette, P.J. Jacques, A. Simar, Critical assessment of the impact of process parameters on vertical roughness and hardness of thin walls of AlSi10Mg processed by laser powder bed fusion, Addit. Manuf. 38 (December 2020) (2021) 101801, http://dx.doi.org/10.1016/j.addma.2020.101801.

[46] J. Damon, S. Dietrich, F. Vollert, J. Gibmeier, V. Schulze, Process dependent porosity and the in fl uence of shot peening on porosity morphology regarding selective laser melted AlSi10Mg parts, Addit. Manuf. 20 (2018) 77–89, http://dx.doi.org/10.1016/j.addma.2018.01.001.

[47] A.D. Plessis, S.G. le Roux, Standardized X-ray tomography testing of additively manufactured parts : A round robin test, Addit. Manuf. 24 (2018) 125–136, http://dx.doi.org/10.1016/j.addma.2018.09.014.

[48] A.D. Plessis, D. Glaser, S. Africa, N.R. Mathe, S. Africa, Pore closure effect of laser shock peening of additively manufactured AlSi10Mg, 3D Print. Addit. Manuf. 6 (5) (2019) 245–252, http://dx.doi.org/10.1089/3dp.2019.0064.

[49] Y. Murakami, M. Endo, Effects of defects, inclusions and inhomogeneities on fatigue strength, Int. J. Fatigue 16 (3) (1994) 163–182, http://dx.doi.org/10.1016/0142-1123(94)90001-9.

[50] S. Tammas-Williams, P.J. Withers, I. Todd, P.B. Prangnell, The influence of porosity on fatigue crack initiation in additively manufactured titanium components, Sci. Rep. 7 (1) (2017) 1–13, http://dx.doi.org/10.1038/s41598-017-06504-5.

[51] I. Tsukrov, M. Kachanov, Stress concentrations and microfracturing patterns in a brittle-elastic solid with interacting pores of diverse shapes, Int. J. Solids Struct. 34 (22) (1997) 2887–2904, http://dx.doi.org/10.1016/S0020-7683(96)00202-8.

[52] G. Kasperovich, J. Haubrich, J. Gussone, G. Requena, Correlation between porosity and processing parameters in TiAl6V4 produced by selective laser melting, Mater. Des. 105 (2016) 160–170, http://dx.doi.org/10.1016/j.matdes.2016.05.070.

[53] T. Vilaro, C. Colin, J.D. Bartout, As-fabricated and heat-treated microstructures of the Ti-6Al-4V alloy processed by selective laser melting, Metall. Mater. Trans. A 42 (10) (2011) 3190–3199, http://dx.doi.org/10.1007/s11661-011-0731-y.

[54] A. Nouri, A. Rohani Shirvan, Y. Li, C. Wen, Additive manufacturing of metallic and polymeric load-bearing biomaterials using laser powder bed fusion: A review, J. Mater. Sci. Technol. 94 (2021) 196–215, http://dx.doi.org/10.1016/j.jmst.2021.03.058.

[55] E.O. Olakanmi, R.F. Cochrane, K.W. Dalgarno, A review on selective laser sintering/melting (SLS/SLM) of aluminium alloy powders: Processing, microstructure, and properties, Prog. Mater. Sci. 74 (2015) 401–477, http://dx.doi.org/10.1016/j.pmatsci.2015.03.002.

[56] B. Vayssette, N. Saintier, C. Brugger, M. El May, E. Pessard, Numerical modelling of surface roughness effect on the fatigue behavior of Ti-6Al-4V obtained by additive manufacturing, Int. J. Fatigue 123 (February) (2019) 180–195, http://dx.doi.org/10.1016/j.ijfatigue.2019.02.014.

[57] G. Lütjering, Influence of processing on microstructure and mechanical properties of ($\alpha + \beta$) titanium alloys, Mater. Sci. Eng. A 243 (1–2) (1998) 32–45, http://dx.doi.org/10.1016/s0921-5093(97)00778-8.

[58] A. Fatemi, R. Molaei, S. Sharifimehr, N. Shamsaei, N. Phan, Torsional fatigue behavior of wrought and additive manufactured Ti-6Al-4V by powder bed fusion including surface finish effect, Int. J. Fatigue 99 (2017) 187–201, http://dx.doi.org/10.1016/j.ijfatigue.2017.03.002.

[59] P. Kumar, U. Ramamurty, Microstructural optimization through heat treatment for enhancing the fracture toughness and fatigue crack growth resistance of selective laser melted Ti–6Al–4V alloy, Acta Mater. 169 (2019) 45–59, http://dx.doi.org/10.1016/j.actamat.2019.03.003.

[60] P. Li, D.H. Warner, A. Fatemi, N. Phan, Critical assessment of the fatigue performance of additively manufactured Ti-6Al-4V and perspective for future research, Int. J. Fatigue 85 (2016) 130–143, http://dx.doi.org/10.1016/j.ijfatigue.2015.12.003.

[61] P. Li, D.H. Warner, J.W. Pegues, M.D. Roach, N. Shamsaei, N. Phan, Towards predicting differences in fatigue performance of laser powder bed fused Ti-6Al-4V coupons from the same build, Int. J. Fatigue 126 (May) (2019) 284–296, http://dx.doi.org/10.1016/j.ijfatigue.2019.05.004.

[62] U. Karr, B. Schönbauer, M. Fitzka, E. Tamura, Y. Sandaiji, S. Murakami, H. Mayer, Inclusion initiated fracture under cyclic torsion very high cycle fatigue at different load ratios, Int. J. Fatigue 122 (November 2018) (2019) 199–207, http://dx.doi.org/10.1016/j.ijfatigue.2019.01.015.

[63] S.C. Wu, Z. Song, G.Z. Kang, Y.N. Hu, Y.N. Fu, The kitagawa-takahashi fatigue diagram to hybrid welded AA7050 joints via synchrotron X-ray tomography, Int. J. Fatigue 125 (March) (2019) 210–221, http://dx.doi.org/10.1016/j.ijfatigue.2019.04.002.

[64] Z. Xu, W. Wen, T. Zhai, Effects of pore position in depth on stress/strain concentration and fatigue crack initiation, Metall. Mater. Trans. A 43 (8) (2012) 2763–2770, http://dx.doi.org/10.1007/s11661-011-0947-x.

[65] M. Banuta, I. Tarquini, Fatigue failure of a drive shaft, J. Fail. Anal. Prev. 12 (2) (2012) 139–144, http://dx.doi.org/10.1007/s11668-012-9551-7.

[66] A.J. Sterling, B. Torries, N. Shamsaei, S.M. Thompson, D.W. Seely, Fatigue behavior and failure mechanisms of direct laser deposited Ti-6Al-4V, Mater. Sci. Eng. A 655 (2016) 100–112, http://dx.doi.org/10.1016/j.msea.2015.12.026.

[67] W. Chi, G. Li, W. Wang, C. Sun, Interior initiation and early growth of very high cycle fatigue crack in an additively manufactured Ti-alloy, Int. J. Fatigue 160 (October 2021) (2022) 106862, http://dx.doi.org/10.1016/j.ijfatigue.2022.106862.

[68] J. Nafar Dastgerdi, O. Jaberi, H. Remes, P. Lehto, H. Hosseini Toudeshky, J. Kuva, Fatigue damage process of additively manufactured 316 L steel using X-ray computed tomography imaging, Addit. Manuf. 70 (January) (2023) 103559, http://dx.doi.org/10.1016/j.addma.2023.103559.

[69] H.K. Rafi, N.V. Karthik, H. Gong, T.L. Starr, B.E. Stucker, Microstructures and mechanical properties of Ti6Al4V parts fabricated by selective laser melting and electron beam melting, J. Mater. Eng. Perform. 22 (12) (2013) 3872–3883, http://dx.doi.org/10.1007/s11665-013-0658-0.

[70] A. Polasik, The Role of Microstructure on High Cycle Fatigue Lifetime Variability in Ti-6Al-4V DISSERTATION Presented in Partial Fulfillment of the Requirements for the Degree Doctor of Philosophy in the Graduate School of The Ohio State University by Alison Polasik (Ph.D. thesis), 2014.

[71] M.T. Hasib, H.E. Ostergaard, Q. Liu, X. Li, J.J. Kruzic, Tensile and fatigue crack growth behavior of commercially pure titanium produced by laser powder bed fusion additive manufacturing, Addit. Manuf. 45 (May) (2021) 102027, http://dx.doi.org/10.1016/j.addma.2021.102027.

[72] H. Galarraga, R.J. Warren, D.A. Lados, R.R. Dehoff, M.M. Kirka, Fatigue crack growth mechanisms at the microstructure scale in as-fabricated and heat treated Ti-6Al-4V ELI manufactured by electron beam melting (EBM), Eng. Fract. Mech. 176 (2017) 263–280, http://dx.doi.org/10.1016/j.engfracmech.2017.03.024.